Physicochem. Probl. Miner. Process., 58(6), 2022, 153509

http://www.journalssystem.com/ppmp

Physicochemical Problems of Mineral Processing

ISSN 1643-1049

Pore structure and surface properties of diatomite with mechanical grinding and its influence on humidity control

Zhibo Hu [1, 2, 3], Shuilin Zheng [4], Jinyu Li [1], Shuaiqian Zhang [1], Min Liu [1], Zhicheng Wang [1], Jiaxin Li [1], Hongjuan Sun [1, 2]

[1] School of Environment and Resource, Southwest University of Science and Technology, Mianyang, 621010, China

[2] Key Laboratory of Solid Waste Treatment and Resource Recycle, Ministry of Education, Southwest University of Science and Technology, Mianyang, 621010, China

[3] Sichuan Provincial Engineering Lab of Non-Metallic Mineral Powder Modification and High-Value Utilization, Southwest University of Science and Technology, Mianyang, 621010, China

[4] School of Chemical and Environmental Engineering, China University of Mining & Technology(Beijing), Beijing, 100083, China

Corresponding author: zhibohu@swust.edu.cn (Zhibo Hu)

Abstract: Mechanical grinding (MG) is an effective method to regulate the pore structure and surface properties of mineral material. Grinding diatomite samples were prepared by horizontal sander under different grinding time. The pore structure and surface properties of grinding samples were characterized systematically by the particle size analysis, low temperature nitrogen adsorption, MIP, fractal theory, XRD, SEM, TEM, FTIR and surface hydroxyl density analysis. The humidity control performance (HCP) of grinding diatomite was tested under different temperature and relative humidity. The relationship among pore structure, surface properties and HCP was analyzed. The results show that macroporous is more easily damaged by mechanical force than mesoporous, and the internal blind holes structure can be opened. The HCP of diatomite is positively correlated with the specific surface area, mesoporous volume, the inhomogeneity of macroporous structure and the number of hydroxyl groups, while negatively correlated with the proportion of macroporous volume.

***Keywords*:** diatomite, mechanical grinding, pore structure, surface properties, humidity control performance

1. Introduction

Energy crisis has become one of greatest problem for human. A high proportion of energy is consumed indoors (Zhong et al., 2019; Fu et al., 2021). According to China Building Energy Consumption Research Report (2019), the total energy consumption of China in buildings accounts for 21.10% of the national total energy consumption. As we know, people spend considerable time living or working indoors, and relative humidity is an important index to evaluate environment comfort (Liu et al. 2021). Air conditioners or humidifiers have been adopted to create suitable relative humidity environment, which need a huge drain on power (Sertsungnern & Chaiwiwatworakul, 2011; Thiangchanta, et al. 2020; Thiangchanta et al., 2021). Humidity control material (HCM) is superior to mechanical humidity control method due to none energy consumption. HCM can regulate environment humidity by adsorb or desorb moisture according to the environment relative humidity. Porous material has the natural advantage of energy storage and mass transfer (Xia et al. 2019; Berger et al. 2021; Yang et al. 2021; Huo et al. 2022).

Diatomite is a kind of natural porous material derived from diatom remains (Mannion, 2012; Yuan et al., 2013). Diatomite is a geological deposit consisting of the fossilised skeletons of numerous species of siliceous marine and fresh water unicellular organisms, particularly diatoms and other algae (Korunic, 1998). Once diatoms died, the organic matter was decomposed, and the frustule was fossilized

DOI: 10.37190/ppmp/153509

and sedimented, which formed deposits of diatomite on sea beds or lakebeds. Geological activity (e.g. volcanic activity) which produces the special environmental conditions can result in the formation of diatomite. These soils consist of individual particles containing intraparticle voids filled with water, resulting in a very unique porous particle morphology (Verdugo, 2008). It is widely used as adsorbent (Al-Degs et al., 2001; Khraisheh et al., 2004; Sheng et al. 2009), filter aid (Seok-Ho et al., 1989; Ha et al., 2015), carrier (Hu et al., 2017c; Zhang et al., 2021), building material (Mingming & Zhang, 2017; Zheng et al., 2017; Shih et al., 2020) and environmental functional material (Du et al. 2011; Quang-Tung et al. 2016; Jiang et al. 2019) for its advantages of high porosity, light mass and nontoxicity. It is widely distributed in the earth. The main mineral compositions of diatomaceous rocks in the Jawornik deposit of Poland are diatoms, quartz, micas, feldspars and glauconite. And the pore structure of these rocks being dominated by macroporous (60–71%) is the closest to that arrived at in the model of cylindrical capillaries with a high degree of complication (Figarska-Warchoł, et al. 2015). The mineralogy and chemical composition of diatomite deposits in central Greece are opal-A, vermiculite, feldspar, quartz, and clay minerals (Stamatakis & Koukouzas, 2001). In our previous research, we also investigated the diatomite from Jilin, Zhejiang and Inner Mongolia of China. The diatom of Jilin diatomite is the shape of a disk. The Inner Mongolia diatomite is boat-shape diatom, while that of Zhejiang diatomite is cylindrical shape diatom (Hu et al. 2017b).

Diatomite is an ideal humidity controlling material owing to its excellent porous feature. Hu et al prepared diatomite/silica composite HCM by partial alkali dissolution using diatomite as silicon source and carrier, and the humidity control ability of composite material improves 4.026 and 7.935 times compared with moisture adsorption and desorption of diatomite (Hu et al., 2017c). These Authors also prepared diatomite/ground calcium carbonate composite HCM with calcination. The 72 h moisture adsorbed amount of composite material improved about 0.46, 0.54 and 0.53-fold as those of diatomite (Hu et al., 2017a). Vu et al prepared HCM by sintering a mixture of diatomite and volcanic ash, and sintered products have excellent moisture adsorption-desorption performances. The products sintered at 1000℃ and 1100℃ have mesoporous structure and the adsorbed moisture contents reach 65 ± 4 g/m2 and 55 ± 2 g/m^2 (Vu et al., 2013). Zheng et al studied the diatomite-based building materials (DBHCBMs), and characterized the porous structure parameters of DBHCBMs and effects of temperature and humidity on performance. The maximum adsorption and desorption content are approximately 12% and 9% of its own weight when the RH is 85%.(Zheng et al., 2017).

The regulation of pore structure and surface properties of porous material can affect the material performance effectively (Hu et al., 2019; Wang et al., 2022; Zhang et al., 2022). Mechanical grinding (MG) is an effective method to obtain appropriate liberation degree which has been widely used in the mineral processing and powder technology. Furthermore, MG can regulate the surface properties and the structure of materials. C Okamura et al prepared single-phase ZnSb thermoelectric materials using mechanical grinding process. The thermal conductivity of the ground materials was 1.41 $Wm^{-1}K^{-1}$ at room temperature, which was lower than that prepared by conventional melt growth and powder metallurgy methods. (Okamura et al., 2010). AG Lehmann et al studied the effect of MG on the hexagonal structure of CdSe (Lehmann et al., 1998). H Imamura et al prepared novel hydrogen storage nano-composites by MG of magnesium and graphite carbon with organic additives, effective nano-composites are those in which there are synergetic interactions between magnesium and graphite as a result of mechanical grinding with the organic additives. and the new hydrogen-storing sites were formed in the composites upon the MG (Imamura et al., 2002). Song et al also studied the hydrogen sorption properties of Mg by reactive mechanical grinding with Cr_2O_3, Al_2O_3 and CeO_2. The hydrogen sorption properties of Mg were improved by mechanical grinding under H_2 (reactive mechanical grinding) with oxides Cr_2O_3, Al_2O_3 and CeO_2 (Song et al., 2002).

At present, there are few researches about regulating of the pore structure and surface characteristics of diatomite the effects by MG. Systematical studies on the pore structure and surface properties of diatomite are necessary to analyze the relationship among the humidity control performance(HCP) of ground diatomite, pore structure and surface characteristics, and further reveal the humidity control mechanism. It is meaningful to guide the synthesis of novel porous HCM in the future. In this paper, the diatomite is mechanically ground to control the pore structure and surface characteristics. The pore structure and surface properties of diatomite were characterized by particle size analysis, low

temperature nitrogen adsorption, mercury intrusion method, the fractal theory, XRD, SEM, TEM, FTIR spectrum and surface hydroxyl density analysis. The HCP of diatomite samples was tested under different temperature and relative humidity.

2. Experiment and Method

2.1. Preparation of samples

The diatomite (DE) was collected from Jilin Province of China, and the diatomaceous type of diatomite ore is disc algae. The SEM image of diatomite ore is shown in Fig. 1. The main chemical components of diatomite were as follows: SiO_2, 87.05%; Al_2O_3, 1.29%; Fe_2O_3, 0.42%; MgO, 0.10%; TiO_2, 0.07%; CaO, 0.01%. 20g diatomite was dispersed in 100ml distilled water with a small amount of sodium hydroxide as dispersant, then the diatomite was grinded for 10min, 30min, 60min, 90min or 120min in a horizontal sander (a novel grinding machine with agitation that grinds various products both continuously and intermittently), using 0.8~1.0mm zirconia as grinding medium, the grinding speed is 1000rpm, zirconia medium filling rate is 60%, and finally the samples were washed, dried and dispersed evenly. The obtained samples were labeled as MK-10, MK-30, MK-60, MK-90, and MK-120, respectively. The diagram of sample preparation procedure is shown in Fig. 2.

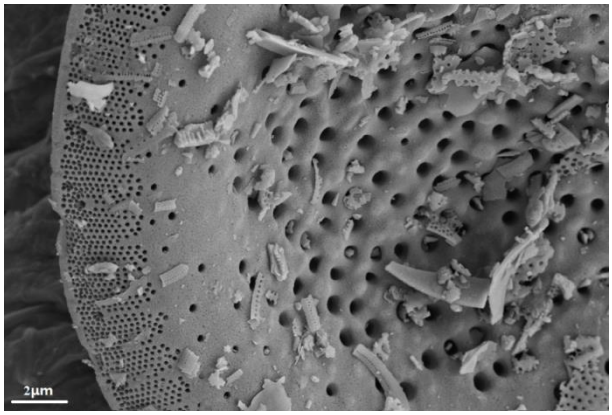

Fig. 1. The SEM image of diatomite

Fig. 2. The diagram of sample preparation procedure

2.2. Characterization

The crystal structure of samples was investigated by XRD diffractometer (Bruker D8 Advance, Germany). Specific surface area, pore volume and pore diameter distribution were characterized with a specific surface area analyzer (Quantachrome Autosorb-iQ, USA) and a mercury porosimeter (Micromeritics AutoPore IV9500, USA). Particle size distribution was analyzed with a laser particle size analyzer (Better BT-2002, China). The fractal dimensions were used to characterize pore surface roughness and pore structure inhomogeneity. The surface morphology was observed by Scanning Electron Microscope SEM (Hitachi S-4800, Japan), and the internal pore structure was analyzed by Transmission Electron Microscopy TEM (Hitachi HT7700, Japan), meanwhile the surface group was

investigated by Fourier Transform Infrared Spectroscopy FTIR (Bruker Vertex70, Germany), and the surface hydroxyl group density was tested by titration.

2.3. HCP

After placing under different temperature and humidity conditions for a period of time, the HCP of the diatomite samples was tested by weighing method according to ISO12571-2006. The moisture content (M) was calculated as follow:

$$M = (m_2-m_1) / (m_1-m_0) \quad (1)$$

where the m_0 is the weight of glass weighing bottle (g), m_1 is the weight of glass weighing bottle with dry diatomite sample (g), m_2 is the weight of glass weighing bottle and diatomite sample with moisture at different test time (g).

3 Result and discussion

3.1 Size analysis

Fig. 3 shows the size analysis results of diatomite samples with the grinding treatment. The size distribution curve and the cumulative size distribution curve of diatomite samples are shown in Fig. 3(a) and Fig. 3(b). The "y" axis in Fig. 3(a) represents the volume proportion of different particle size of diatomite. The Fig. 3(c) shows the D50 and D95 of diatomite samples versus grinding time. The size distribution width of diatomite samples is shown in Fig. 3(d).

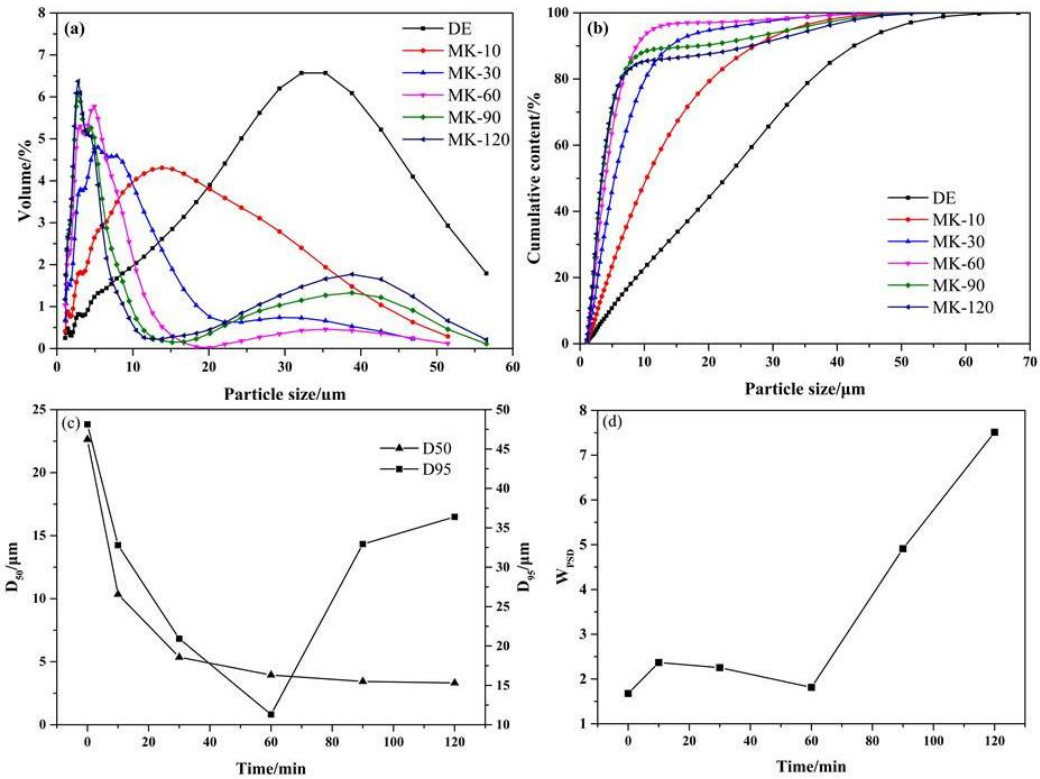

Fig. 3. Distribution curves of diatomite particle size at different grinding time(a: particle size distribution curve; b: cumulative particle size distribution curve), evolution of particle size (D_{50} and D_{95}) of diatomite samples versus grinding time(c), PSD curves of diatomite samples at different grinding time(d)

The particle size distribution intervals of grinding diatomite samples were up to 60 μm. As the grinding time is extended, particle size distribution curves presented a trend from the unimodal distribution to the bimodal distribution. When the grinding time was less than 30min, the size distribution curve of diatomite showed a single peak distribution, and the maximum size sharply decreased from 35.350μm (DE) to 5.413μm (MK-30). The size distribution of MK-60 showed a bimodal

distribution curve, and the two peaks appeared at the particle size of 3.083μm and 35.350μm, respectively. The size distribution curve of diatomite still showed a bimodal distribution, while the integral area of peak of particle size of 3.083μm decreased with the increasing of grinding time. The corresponding pore size of the peak decreased from 3.083μm (MK-60) to 2.806μm (MK-120) in Fig. 3(a), and the particle volume proportion increased from 5.30% (MK-60) to 6.37% (MK-120). The integral area of the larger pore of peak presented an increasing trend. The corresponding pore size of the peak increased from 35.350μm (MK-60) to 38.380μm (MK-120).Seen from Fig. 3(c), D_{50} showed a continuous decreasing trend with the prolongation of the grinding time. D_{50} decreased obviously within 30min. When the grinding time exceeded 30min, the D_{50} decreased slightly. D_{50} basically remained stable if the grinding time exceeded 90min. D_{95} firstly rose and then declined with the increasing of grinding time. And D_{95} reached the minimum value of 11.310μm when the grinding time was 60min. D_{95} increases when the grinding time exceeds 60min may be due to the agglomeration of mechanochemical effect (Ai et al., 2018; Peddarasi & Sarkar, 2021). Some particle gather, and the particle size of diatomite become larger. The aggregation of small particles results in a grinding equilibrium. It is related to the high surface energy and specific surface area. The size distribution width was calculated according to formula $W_{PSD}=(D_{90}-D_{10})/D_{50}$. Seen from Fig. 3(d), the size distribution width firstly increased then decreased and finally increased again with the prolonging of grinding time. When the grinding time exceeded 60min, the size distribution width rapidly increased from 1.810 (MK-60) to 7.510 (MK-120), which was increased more than 4 times. The difference of particle size of diatomite become more obviously. The size distribution width of diatomite can be remarkably affected by grinding treatment.

3.2. Nitrogen adsorption

Nitrogen adsorption is widely used to characterize the pore structure. Fig. 4 shows the nitrogen adsorption-desorption isotherms of diatomite samples. Fig.4 show the nitrogen adsorbed volume ("Y" axis) of grinding diatomite as the change of relative pressure ("X" axis).

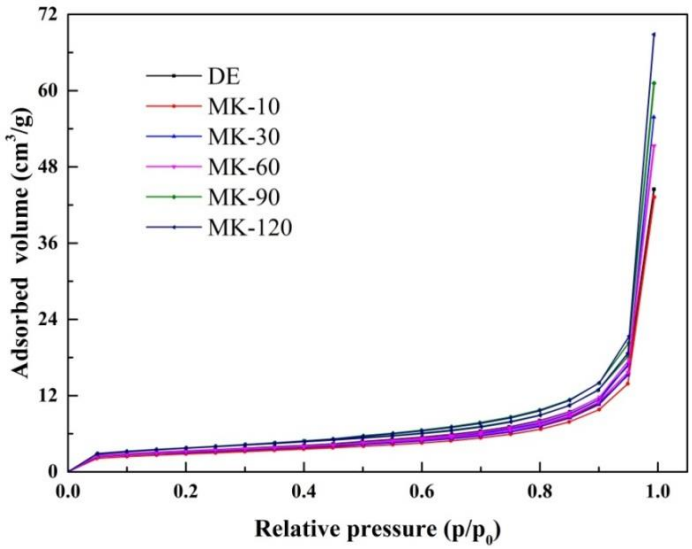

Fig. 4. Nitrogen adsorption-desorption isotherms for diatomite samples at liquid nitrogen gas temperature (77K)

The isothermal were IV type curves according to IPUAC (International Union of Pure and Applied Chemistry). There are obvious hysteretic loops in the p/p0 range of 0.6~0.9, and the shape and size of hysteretic loops of diatomite samples are similar to each other, which indicate that there are mesoporous in the diatomite samples and mechanical grinding has no significant effect on the mesoporous structure. The nitrogen adsorption capacity of the diatomite samples was small at low relative pressure ($p/p_0 < 0.1$), indicating that no microporous structure existed in the diatomite. There were no high platforms at high relative pressure ($p/p_0 > 0.9$), thus there are macroporous structures in the diatomite. The nitrogen adsorption capacity decreased from 44.487cm^3/g (DE) to 43.241cm^3/g (MK-10) and then increased to 61.169cm^3/g (MK-90) at the p/p0 of 0.995 with the increasing of grinding time.

Table 1. Pore structure parameters of DE, MK-10, MK-30, MK-60, MK-90 and MK-120 by low temperature nitrogen gas adsorption

Sample	SSA /(m^2/g)	SSA_{mic} /(m^2/g)	V_T /(cm^3/g)	V_{mic} /(cm^3/g)	V_{mes} /(cm^3/g)	D_a /(nm)
DE	11.390	1.868	0.069	0.001	0.068	24.150
MK-10	10.041	1.330	0.067	0.001	0.066	26.639
MK-30	10.915	2.144	0.086	0.001	0.085	31.652
MK-60	11.468	2.356	0.079	0.001	0.078	27.698
MK-90	13.430	1.723	0.095	0.001	0.094	28.177
MK-120	13.224	1.647	0.107	0.001	0.106	32.208

Table 1 shows the main pore structure parameters of the diatomite samples analyzed by the low-temperature nitrogen adsorption. The nitrogen adsorption capacity of the diatomite is positively correlated with the specific surface area (SSA). SSA decreased from 11.390m2/g (DE) to 10.041m2/g (MK-10) and then increased to 13.430m2/g (MK-90). The change of SSA may be correlated with the destruction of macroporous and opening of new mesoporous.

The total pore volume (VT) of the samples decreased firstly and then increased as the prolongation of grinding time. The VT of MK-120 (0.107cm3/g) was significantly higher than that of DE (0.069cm3/g). The results showed that the mesoporous (2~50nm) structure in the diatomite was not damaged obviously within short mechanical grind time, as the result of Vmes of MK-10 shown. As the grinding time extended, the blind pore structure in the diatomite with pore size of 2-50nm was maybe opened, and the total mesoporous volume was increased. The microporous structure was analyzed using T-plot method, and the results are shown in Table 1. All of the microporous volumes of diatomite samples were 0.001cm3/g, which confirmed that there was basically no microporous.

Fig. 5 shows the distribution curve of SSA and pore size of diatomite samples analyzed by BJH model and DFT model. Seen from Fig. 5(a), the analysis results of BJH model showed that the differential surface area of diatomite decreased as the pore size increased, which indicated that the pore with smaller size had a greater effect on the SSA. The differential SSA of the same pore size range decreased firstly and then increased with the extension of grinding time, and the dS/dD of MK-90 was larger than those of other samples in each pore size range. Seen from Fig. 5(b), the DFT model SSA distributions of diatomite samples showed a bimodal distribution, located within the range of 5-20nm and 25-50nm, respectively. When the pore size was located in 5-20nm, the variation of differential SSA of each pore size was basically coincide with the analysis results of BJH model. When the pore size was 25-40nm, the differential SSA of pore size gradually increased with the extension of grinding time, while the variation amplitude was larger than that of pore size located in 5-20nm.

Seen from Fig. 5(c), the BJH pore size distribution of diatomite samples had a wide peak in the range of 5-20nm. The pore size of the peak center moved left or right without obvious regularity as grinding time extended. The differential dV/dD pore volumes of mesoporous (Vmes) decreased firstly and then increased with the extension of grinding time, which was consistent with the Vmes results presented in Table 1 column6. The DFT model pore distribution of diatomite samples (Fig. 5(d)) showed a bimodal distribution, located in the pore size range of 5-20nm and 25-50nm, respectively. The Vmes of pore size range of 25-50nm were larger than those of 5-20nm. The differential pore volumes gradually increased with the extension of grinding time, and the pore volumes with pore sizes of 25-50nm were larger than those of 5-20nm. The increase of pore volumes is probably related to the opening of the blind pores by MG.

3.3 Mercury Intrusion Porosimetery (MIP)

Fig. 6(a) shows the cumulative Mercury Intrusion Porosimetery curves and Fig 6(b) presents the pore size distribution curves of diatomite samples analyzed by MIP.

As the intake pressure increased, mercury successively entered the macroporous and mesoporous. Seen from Fig. 6(a), the cumulative mercury intrusion curves increased rapidly when the pressure was

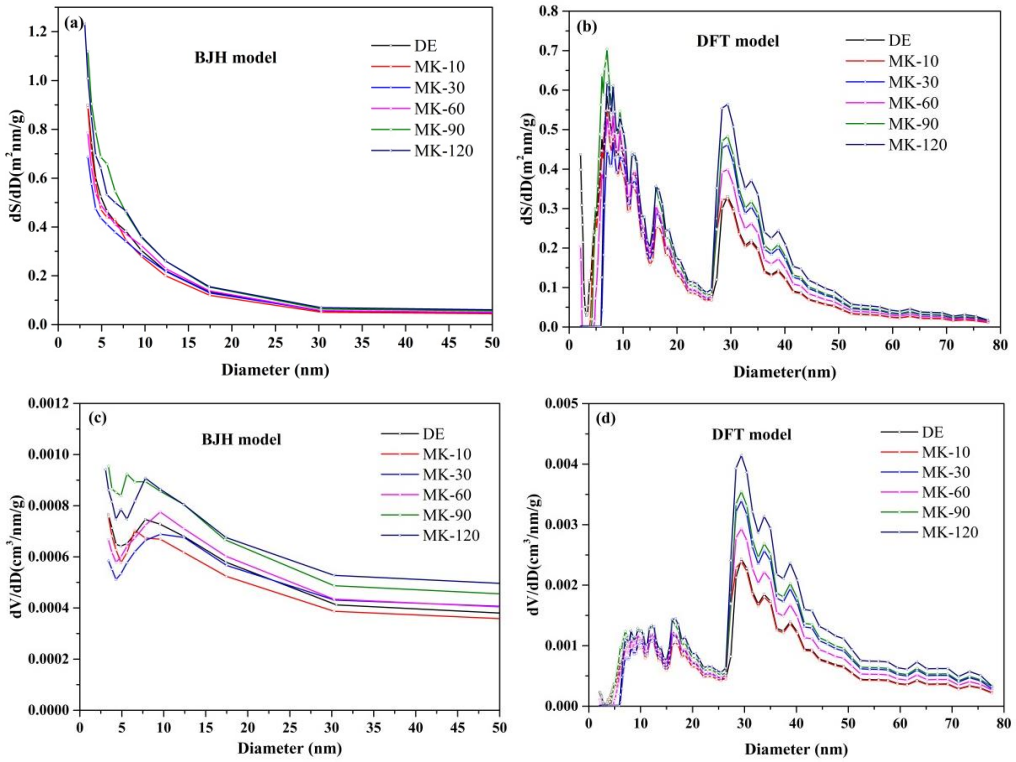

Fig. 5. Specific surface area distributions isotherms (a, b) and pore volume distribution isotherms(c, d) of diatomite samples

50-500pa. When the mercury pressure was less than 10pa or larger than 1000pa, the mercury intrusion volume was almost constant. Seen from Fig. 6(b), the pore size distribution of diatomite samples presented a bimodal distribution on the whole. The pores size was mainly located in the range of 50-4000nm and 10000nm. The former were the inner pores of the diatomite, while the latter were the pores piled between the diatomite particles. The peak areas of the pores between the diatomite particles were much smaller than those of the pores of diatom, thus the volume between diatomite particles do not influence the cumulative pore volume. As the grinding time extended, the peak value of pore in the diatom increased firstly then decreased, and the pore diameter moved to the smaller one. Grinding time can affect the macroporous remarkably.

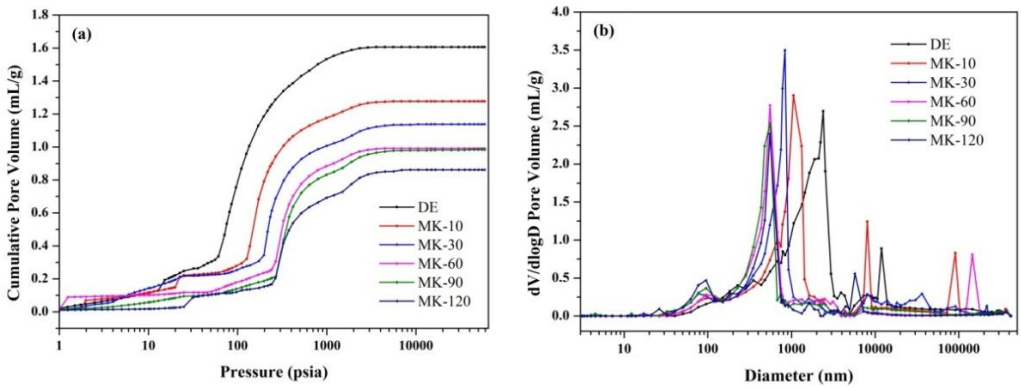

Fig. 6. Cumulative intrusion vs pressure (a) and pore volume distribution with pore size (b) derived from of diatomite samples using MIP

Table 2 shows the pore structure parameters of the diatomite samples analyzed by MIP. The Vintr decreased gradually with the destruction of macroporous structure during the mechanical grinding. The Vintr of DE was the largest, which reached 1.606 mL/g. Seen from Table 2, the VD＜0.05 μ m is not more than 0.020ml/g, thus the mercury basically did not enter the pore structure with pore size less

than 50nm. Combined with the results of size analysis in section 3.1, the size of diatomite particles treated by mechanical grinding was less than 60μm, and VD > 10μm presented the volume between the diatomite particles, which was invalid volume for the macroporous of diatomite. The macroporous of diatomite were mainly between 50nm and 5000nm, which accounted for 89.86-98.75% (these values are not identified in table 2, row VE) of the effective mercury intrusion volume (VE). As the grinding time increased, the macroporous volume generally increased except MK-60 in the pore size range of 0.050~0.100μm, while the pore volume in the pore size range of 100-1000nm increased firstly and then decreased. The macroporous volumes with pore diameters from 1000nm to 5000nm decreased. These results showed that the macroporous with pore size from 1000nm to 5000nm were damaged more easily by mechanical force than those with pore size of 50-100nm. The threshold aperture (Df, which is the inflection point of cumulative mercury intrusion curve) and average pore size (DV) decreased with the increasing of grinding time. Combined with Vmes, it can be seen that the ratio of VE and the macroporous volume ratio (Φ) decreases gradually with the extension of grinding time.

Table 2. Pore structure parameters of diatomite samples by MIP

Parameters	DE	MK-10	MK-30	MK-60	MK-90	MK-120
Vintr /(ml/g)	1.606	1.277	1.138	0.992	0.984	0.862
$V_{D>10\mu m}$/(ml/g)	0.209	0.144	0.185	0.110	0.081	0.024
$V_{5\mu m<D<10\mu m}$/(ml/g)	0.054	0.084	0.035	0.008	0.019	0.069
$V_{1\mu m<D<5\mu m}$ /(ml/g)	0.865	0.456	0.088	0.108	0.080	0.052
$V_{0.1\mu m<D<1\mu m}$ /(ml/g)	0.459	0.555	0.762	0.730	0.731	0.631
$V_{0.05\mu m<D<0.1\mu m}$ /(ml/g)	0.018	0.033	0.054	0.033	0.055	0.070
$V_{D<0.05\mu m}$ /(ml/g)	0.000	0.006	0.015	0.003	0.019	0.017
V_E/(ml/g)	1.397	1.127	0.938	0.879	0.884	0.821
D_f/nm	2534.500	1319.400	834.900	677.900	553.100	553.300
Φ/%	95.293	94.386	91.602	91.754	90.296	88.470
D_V/nm	1782.200	1089.300	784.7800	583.000	521.500	543.100

Note: Microporous, pore size less than 2nm; Mesoporous, pore size between 2nm to 50nm; Macroporous, pore size larger than 50nm

3.4. Fractal characteristics

The isothermal adsorption and desorption curves of grinding diatomite samples (Fig. 4) have two obvious linear regions within the range of relative pressure p/p0 =0-0.35 and p/p0 =0.35-1.0. Fig. 7(a) shows diatomite samples subsection fitting results by FHH model. Table 3 shows the linear fitting equation, fractal dimensions (DF1 and DF2, which can quantitative evaluate the fractal characteristics.) and fitting correlation coefficient (R2) of the pores of grinding diatomite samples in the pore size range of 2~50nm. Fig. 7(b) and Fig. 7(c) are the fitting results of fractal characteristics of macroporous pores of diatomite samples by Menger sponge model and thermodynamic relationship model, respectively. Table 4 presents the linear fitting equations and fractal dimensions (a ratio providing a statistical index of complexity comparing how detail in a fractal pattern changes with the scale at which it is measured). (DM and DT) and fitting correlation coefficients (R2) of the pores of diatomite sample in the pore size range of 50-5000nm.

Table 3 Fractal dimensions of diatomite samples derived using fractal FHH method

Sample	p/p_0=0-0.35			p/p_0=0.35-1.0		
	D_{F1}	FHH model	R_{F1}^2	D_{F2}	FHH model	R_{F2}^2
DE	2.60	$y_1=-0.40x_1+1.36$	1.00	2.52	$y_2=-0.48x_2+1.31$	1.00
MK-10	2.56	$y_1=-0.44x_1+1.24$	1.00	2.51	$y_2=-0.49x_2+1.19$	1.00
MK-30	2.61	$y_1=-0.39x_1+1.32$	1.00	2.46	$y_2=-0.54x_2+1.22$	0.99
MK-60	2.60	$y_1=-0.40x_1+1.37$	1.00	2.49	$y_2=-0.51x_2+1.29$	1.00
MK-90	2.57	$y_1=-0.43x_1+1.53$	1.00	2.50	$y_2=-0.50x_2+1.47$	1.00
MK-120	2.57	$y_1=-0.43x_1+1.52$	1.00	2.47	$y_2=-0.53x_2+1.43$	1.00

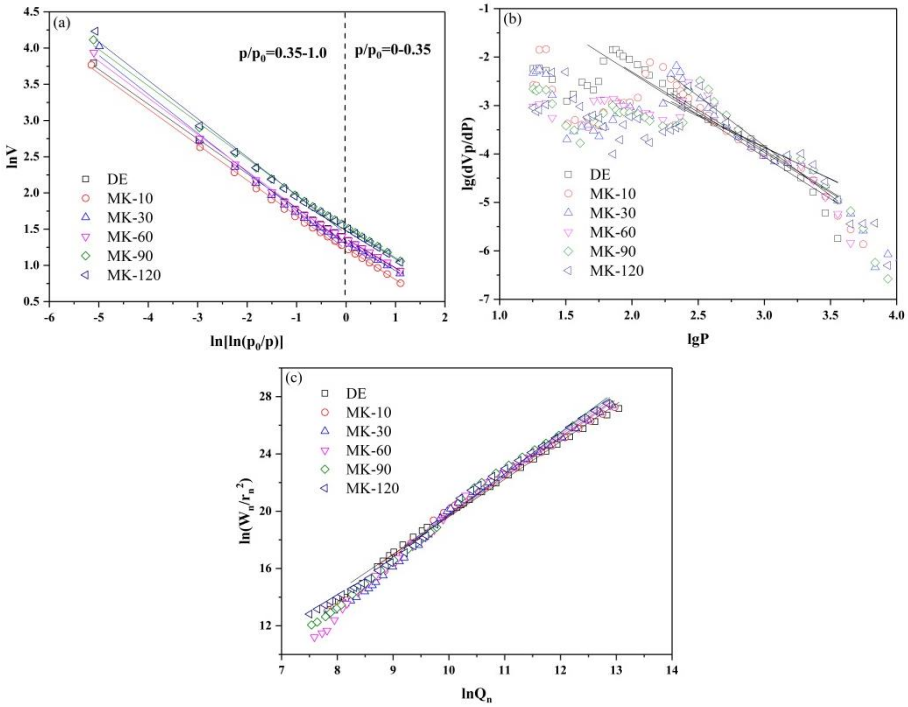

Fig. 7. A plot of lnV vs. ln[ln(p0/p)] (FHH model)(a), a plot of lg(dVp/dP) vs. lgP (Menger sponge model)(b), a plot of ln(Wn/rn2) vs. lnQn (thermodynamics correlation model)(c)

Table 4. Fractal dimensions of diatomite samples derived using fractal Menger sponge model and thermodynamics correlation model

sample	Menger model	D_M=4+A	R_M^2	thermodynamics correlation model	D_T	R_T^2
DE	y=-1.73x+1.13	2.27	0.90	y=2.62x-6.58	2.62	0.99
MK-10	y=-1.66x+1.02	2.34	0.87	y=2.71x-7.45	2.71	0.99
MK-30	y=-2.05x+2.33	1.95	0.96	y=2.71x-7.35	2.71	0.99
MK-60	y=-1.69x+1.13	2.31	0.79	y=2.73x-7.54	2.73	0.99
MK-90	y=-1.29x+0.01	2.71	0.66	y=2.82x-8.46	2.82	0.99
MK-120	y=-1.33x+0.14	2.67	0.72	y=2.90x-9.25	2.90	0.99

The fitting results showed that the fractal characteristics of the diatomite had a good fitting degree in the two regions, the value of R2 was greater than 0.99. The fitting results showed that the diatomite samples had different fractal characteristics in the two intervals. Refer to the relevant literature and previous researchers' studies, DF1 and DF2 reflect the surface roughness and inhomogeneity of mesoporous volume, respectively (Sonwane et al. 1999; Pyun et al. 2003; Vilchis-Granados et al. 2013). Table 3 shows the fractal dimensions calculated according to the fitting results in Fig. 7(a). DF1 and DF2 showed irregular changes with the extension of grinding time, which may be due to the irregular variation of newly generated surfaces. DF1 fluctuated between 2.56 and 2.61. The effect of MG was not significant on DF1. It is possibly due to that the macroporous structure was broken by MG. The holes wall of the macroporous is close to the plane, and the new generated section is relatively flat, thus it has no significant influence on DF1. DF2 varied in the range of 2.46-2.52, which was related to variation of the mesoporous by MG. The change of mesoporous inhomogeneity maybe affect by the loss of partial mesoporous during the grinding and the opening of internal blind holes.

Seen from Table 4, the DM was less than DT for the same sample. The DM did not change regularly with the increase of grinding time, and the value of DM did not satisfy the range of the fractal dimension, which is located from 2 to 3. The fractal dimensions of thermodynamic relationship model increased gradually with the increasing of grinding time, and the value of DT was between 2.6 and 2.9. All of RT2 values were greater than 0.99, indicating that the reliability of thermodynamic relationship

model is superior to Menger sponge model. The macroporous structure complexity of diatomite increases with the prolongation of grinding time, and MG can break the orderliness of macroporous structure.

3.5. Morphology analysis

The surface morphology analysis results of the diatomite samples are shown in Fig. 8. And Fig. 9 shows TEM results of diatomite samples.

Seen from the low magnification (x2000) SEM, the natural diatomaceous soil usually has a proportion of breakage (Fig. 8 (a)), and there were only a few intact diatoms after grinding 10min (Fig. 8 (b)). As the grinding time extended, diatoms were ground into irregular lumps. When the grinding time exceeded 90min, the difference of size and shape of diatomite particle was small under SEM images (Fig. 8 (e)). The single diatomite particles with different grinding time were analyzed with high magnification (x5000) SEM, and the porous structure was observed. The side pore structure of MK-90 was appeared, which was due to the opening of the blind holes by MG. Seen from Fig. 9, the destruction of mesoporous structures was not obvious by MG. Grid-like mesoporous structures were observed in MK-10 and MK-90. The internal mesoporous surface of MK-120 was irregular, which can increase the SSA of grinding diatomite, as Table 1, Column2 shown.

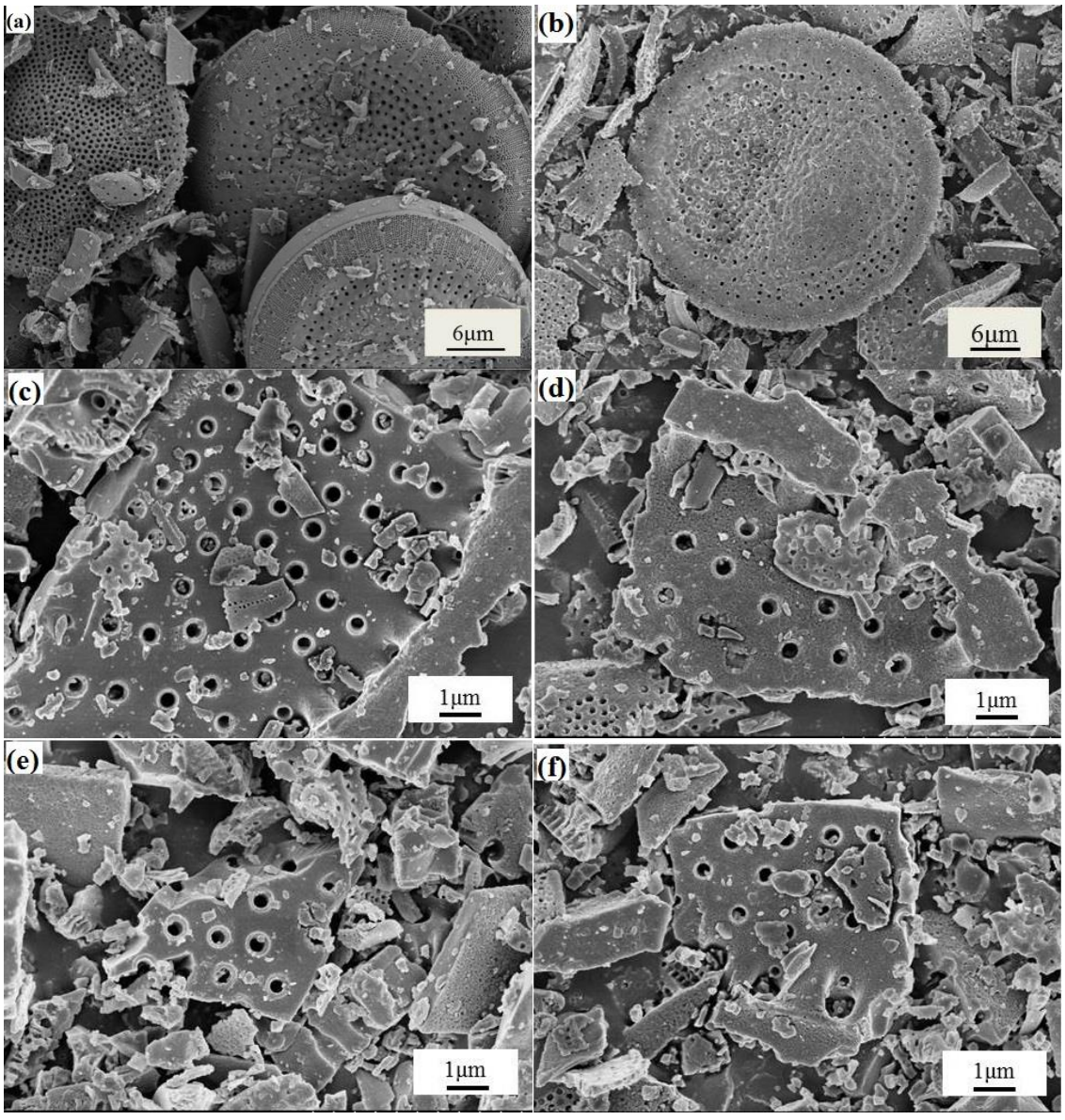

Fig. 8. SEM images of DE (a), MK-10 (b), MK-30 (c), MK-60 (d), MK-90(e) and MK-120 (f)

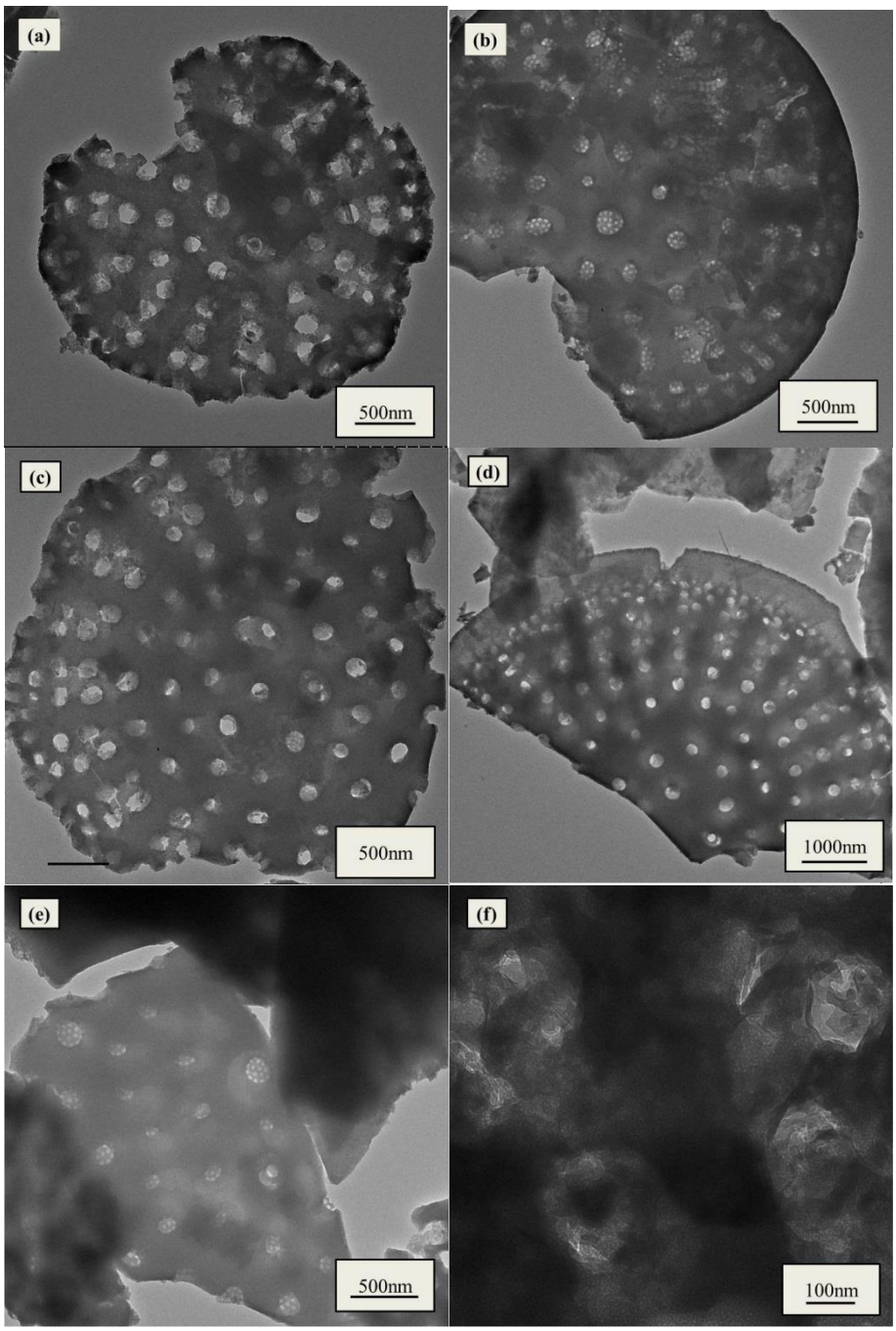

Fig. 9. TEM images of DE (a), MK-10 (b), MK-30 (c), MK-60 (d), MK-90(e) and MK-120 (f)

3.6. XRD and surface group analysis

Fig. 10(a) shows the X-ray diffraction results of diatomite samples. Fig. 10(b) shows the FTIR spectra of DE, MK-10, MK-90 and MK-120. Fig. 10(c) shows the surface hydroxyl density test results of diatomite samples, which can reflect the amount of hydroxyl of unit area on the surface of diatomite.

MG did not influence the crystal structure and mineral composition of diatomite. The peaks of amorphous silica have not been changed in the 2θ range of 15-35°. Diatomite contained a small amount of impurities such as quartz, mica and feldspar. Vibration peaks appeared in the bands of 1097cm-1 were the stretching vibration peak of Si-O bond, Vibration peaks appeared in the bands of 800 cm-1 were the stretching vibration peak of symmetric Si-O bond and the deformation vibration peak of Si-O-Si amorphous SiO2 appeared in the bands of 465 cm-1 in the four samples, (Mu et al. 2018; Li et al. 2019; Wu et al. 2021). As the content of SiO2 had not been changed during the grinding process, the strength

of the vibration peak of Si-O bond basically remained unchanged. The strength of surface isolated hydroxyl group at 3745cm-1, the vibration band of hydroxyl group adsorbed water at 3446cm-1 and the characteristic peak of O-H deformation vibration at 1643cm-1 were gradually weakened, which may be related to the gradual decrease of the macroporous structure in the grinding process. It can be seen that the surface hydroxyl density increased firstly and then decreased with the increasing of grinding time. New fracture surface may have a certain amount of hydroxyl, which increases the number of hydroxyl group content of unit area. Surface hydroxyl density reduced with the increasing of grinding time, which may be due to the damage of surface hydroxyl.

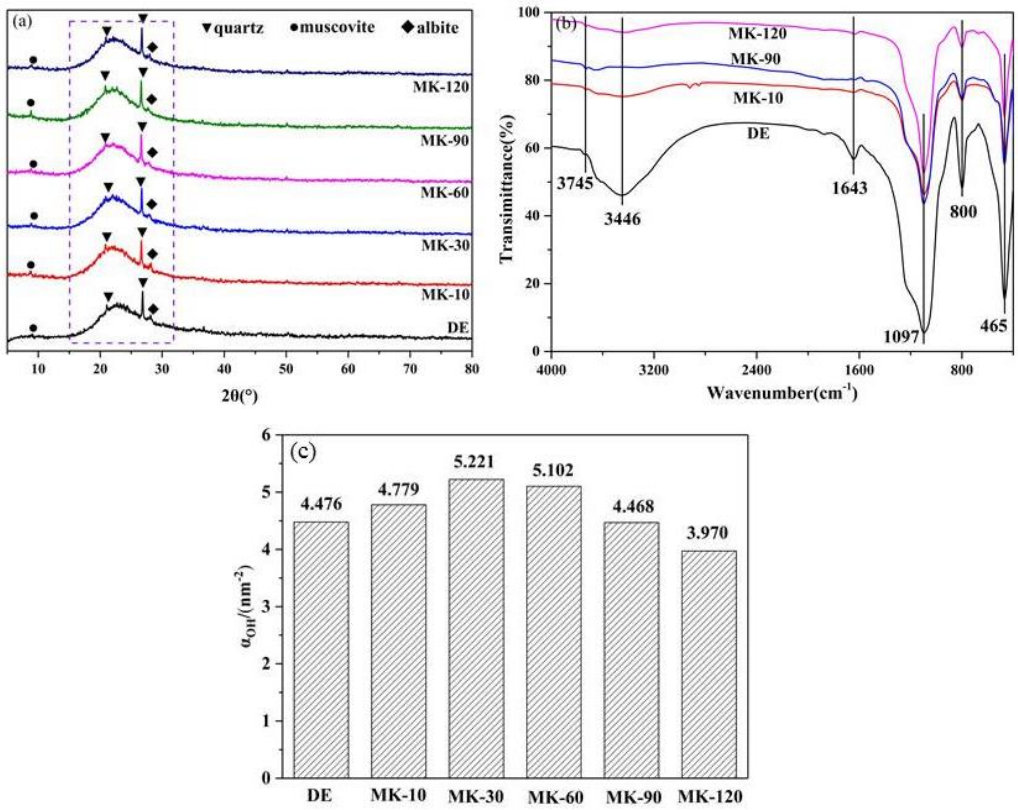

Fig. 10. XRD and surface group analysis. (a) XRD patterns; (b) FTIR spectra; (c) Surface hydroxyl density

3.7. HCP

Fig. 11 shows the HCP curves of diatomite samples at different relative humidity. It can be seen that in the initial stage diatomite samples have a relatively fast hygroscopic rate. As the hygroscopic time lengthened, the hygroscopic rate gradually decreased and the moisture adsorption equilibriums were basically reached at 72h. At the same temperature (20℃), the 72h humidity control ability of MK-90 were 9.19%(98%RH), 6.84%(85%RH) and 5.85%(75%RH) while those of DE were 7.96%, 5.71% and 5.24%, respectively. The moisture absorption capacity basically increases with the prolongation of grinding time. The moisture desorption curves of diatomite with different grinding time were basically stable after 12h, and the desorption process was much easier to reach balance than adsorption process. The 72h moisture release contents of DE were 3.14% (98%RH-33%RH), 1.52% (85%RH-33%RH) and 1.20% (75%RH-33%RH), while those of MK-90 increased to 4.27%, 1.89% and 1.20%, respectively. The moisture desorption increases with the lengthening of grinding time. The moisture absorption and desorption rule fluctuated slightly when the grinding time was 10min or 120min. At the same temperature, the moisture absorption of diatomite samples increases as the increase of environmental relative humidity, and the moisture desorption increase as the difference of environmental relative humidity increase.

Fig. 12 shows the humidity control curves of diatomite samples at different temperatures. It can be seen that under the same environmental relative humidity, 72h moisture absorption content of

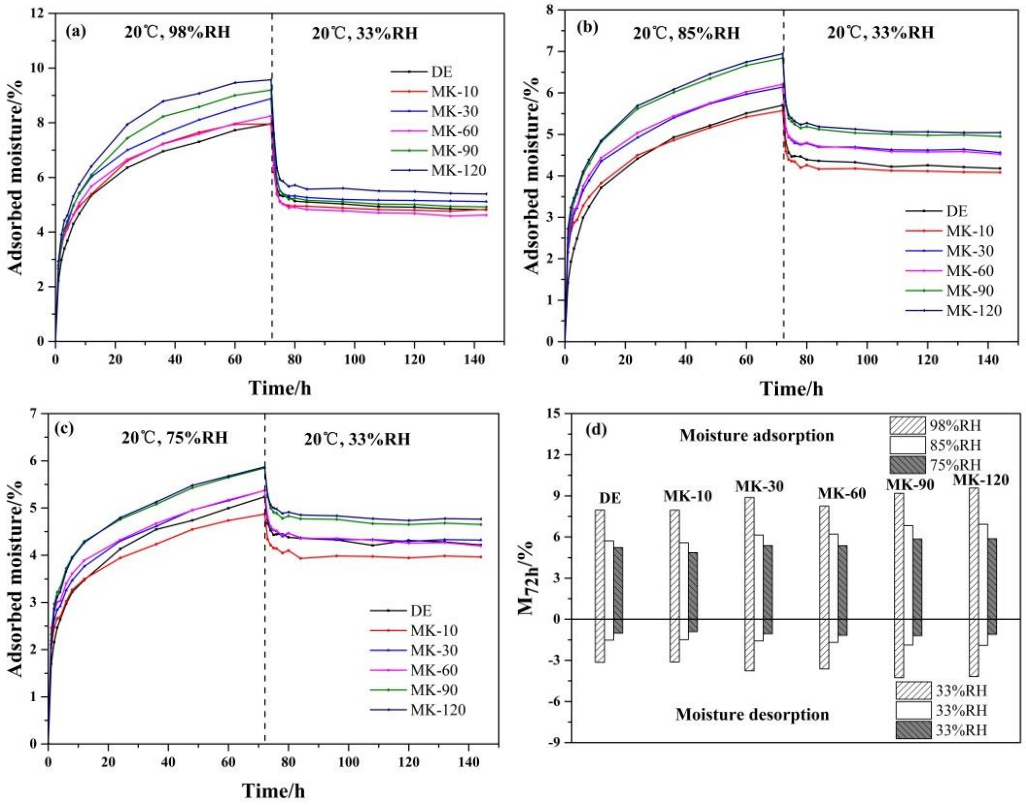

Fig. 11. Moisture adsorption-desorption performance of diatomite samples under different relative humidity (a: 98%RH-33%RH; b: 85%RH-33%RH; c: 75%RH-33%RH; d: 72h)

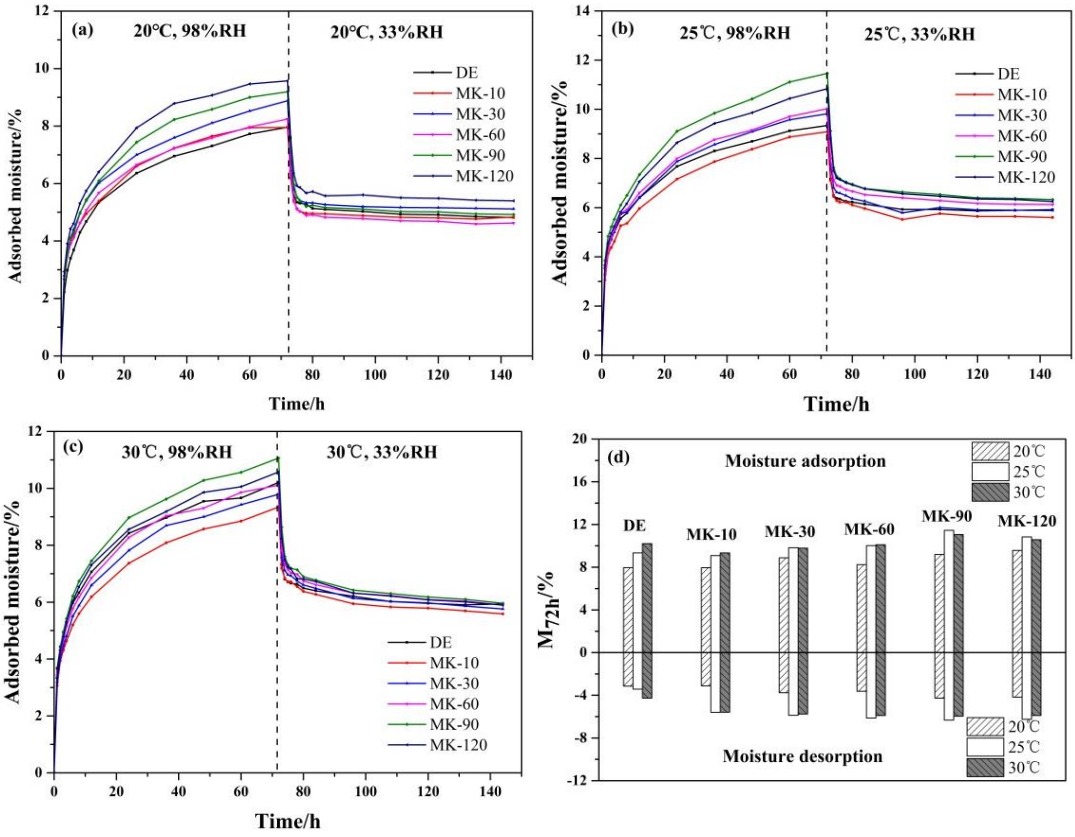

Fig. 12. Moisture adsorption-desorption performance of diatomite samples under different temperature (a: 20℃; b: 25℃; c: 30℃; d: 72h)

diatomite increased as the ambient temperature increased. Under the same environmental relative humidity difference, the 72h moisture desorption content of diatomite basically increased with the increase of ambient temperature. The 72h moisture absorption contents of DE under 98% RH were 7.96% (20℃), 9.34% (25℃) and 10.21% (30℃), and those of MK-90 increased to 9.19%, 11.46% and 11.06%, respectively. The moisture absorption capacity basically increased with the prolongation of grinding time. When environmental relative humidity dropped to 33%, the 72h moisture desorption contents of DE were 3.14% (20℃), 3.42% (25℃) and 4.26% (30℃), while those of MK-90 increased 4.27%, 6.33% and 5.96%, respectively. The moisture desorption rate basically increased with the prolongation of grinding time. The moisture absorption and desorption rule also fluctuated slightly when the grinding time was 10min or 120min. Seen from the relation diagram (Fig. 13) of the equilibrium moisture absorption content and equilibrium moisture desorption content of diatomite samples under different temperature and relative humidity conditions, it reveals that the moisture desorption of the diatomite samples are positively correlated with moisture absorption. The moisture desorption performance is determined by the moisture adsorption performance.

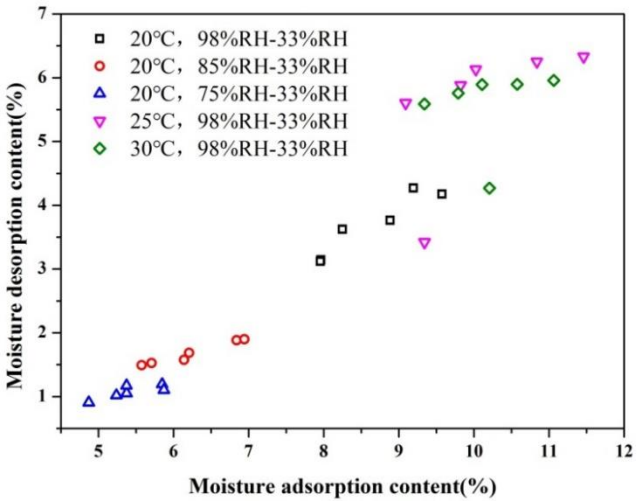

Fig. 13. The relationship of moisture adsorption performance and moisture desorption performance of grinding diatomite samples under different temperature and relative humidity

3.8. Relationship among pore structure, surface characteristics and HCP

Fig. 14 shows the relationship among pore structure, surface characteristic parameters and the HCP of diatomite samples.

HCP has a positive correlation with V_T, SSA, D_T and number of surface hydroxyl groups ($S \bullet \alpha_{OH}$),while it has negative relation with D_{50}, VE and ratio of macroporous volume Φ. The D_{95}, D_a of the mesoporous, D_f, DF_1 and DF_2 have no direct relationship with the humidity control performance.

A larger SSA could increase the probability of collision between water vapor molecules and diatomite. Meanwhile, it could provide more active sites for adsorption and increase the probability of water molecules adhering to the diatomite surface(Li et al. 2022; Xiao et al. 2022). The surface fractal dimension DF1 fluctuated around 2.60 and had little correlation with the humidity control performance. The fractal dimension DF_2 of mesoporous pores is basically maintained around 2.50, and the heterogeneity of mesoporous volume is basically stable, which has no great influence on the humidity control performance. As the grinding time extended, partial macroporous structure were gradually destroyed, internal macroporous with smaller pore size and part of the blind hole were opened, the macroporous inhomogeneity increased, which reduced the distance of water vapor molecules into the pore, and enhanced the humidity control properties of diatomite. The graph of the process is shown in Fig. 15. The smaller the proportion of macroporous volume is, the better the humidity control performance is. The HCP of macroporous is lower than that of mesoporous structure. New surface hydroxyl groups were generated when diatomite was ground into fragments, which further enhanced the HCP. New pore structures and surfaces have been developed in the diatomite by MG, thus the internal pores can directly contact with water vapor, which improves the HCP.

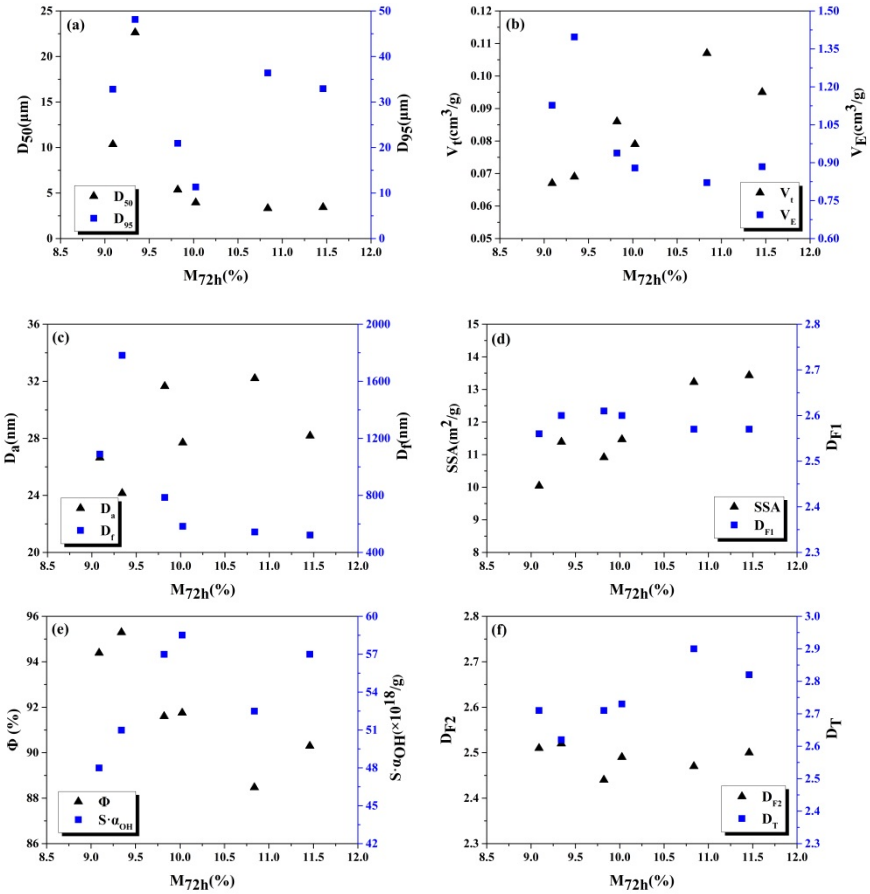

Fig. 14. The relationship image of porous intersurface properties and humidity control performance of diatomite samples.((a)D_{50} and D_{95}; (b)Vt and VE; (c) D_a and D_f; (d) SSA and DF1; (e) Φ and S•αOH; (f)DF_2 and DT)

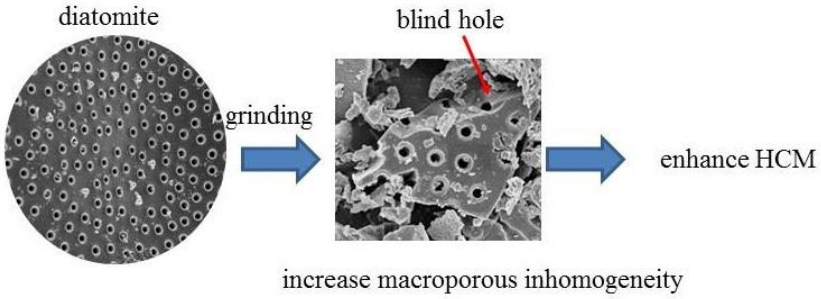

Fig. 15. The graph of grinding process of diatomite and HCM

4. Conclusion

MG does not influence the crystal structure of diatomite, and the macroporous is more easily damaged by mechanical force. The internal blind pore can be opened, which increased the specific surface area and mesoporous. The influence of mesoporous is greater than macroporous on SSA of diatomite. As the grinding time prolonged, the particle size and macroporous volume proportion decreased, while the macroporous fractal dimensions, macroporous surface roughness and nonuniformity increases. The fractal dimension of mesoporous pores has not been significantly changed, and the hydroxyl density on the surface increases first and then decreases.

The pore structure and surface characteristics of diatomite have significant effect on the humidity control ability. The SSA, mesoporous volume, the proportion of macroporous volume, the inhomogeneity of macroporous structure and the number of hydroxyl groups on the surface are important factors that determine the humidity control capacity of diatomite. The HCP of diatomite is

positively correlated with the specific surface area, mesoporous volume, the inhomogeneity of macroporous structure and the number of hydroxyl groups, while negatively correlated with the proportion of macroporous volume.

Acknowledgement

We are grateful for the support from the National Science Foundation of China (Grant Nos.51804262).

References

AI Z., LIU C., ZHANG Q., QU J., LI Z., HE X., 2018. *Adding ZnO and SiO2 to scatter the agglomeration of mechanochemically prepared Zn-Al LDH precursor and promote its adsorption toward methyl orange*. Journal of Alloys and Compounds 763, 342-8.

AL-DEGS Y., KHRAISHEH M., TUTUNJI M.F., 2001. *Sorption of lead ions on diatomite and manganese oxides modified diatomite*. Water Research 35, 3724-8.

BERGER J., LEGROS C., ABDYKARIM M., 2021. *Dimensionless formulation and similarity to assess the main phenomena of heat and mass transfer in building porous material.* Journal of Building Engineering 35, 101849.

DU Y., SHI S., DAI H., 2011. *Water-bathing synthesis of high-surface-area zeolite P from diatomite*. Particuology 9(2), 174-178.

FIGARSKA-WARCHOŁ B., STAŃCZAK G., REMBIŚ M., TOBOŁA T., 2015. *Diatomaceous rocks of the Jawornik deposit, the Polish Outer Carpathians. - petrophysical and petrographical evaluatio*n. Geology, Geophysics, Environment 41, 311-31.

FU H., BALTAZAR J.-C., CLARIDGE D.E., 2021. *Review of developments in whole-building statistical energy consumption models for commercial buildings*. Renewable and Sustainable Energy Reviews 147, 111248.

HA J-H, BAE B, SONG I-H,2015. *Effect of pore characteristics on permeability of sintered diatomite filter for microfiltration.* Advances in Applied Ceramics 114(3), 156-163

HU Z.-P., REN J.-T., YANG D., WANG Z., YUAN Z.-Y., 2019. *Mesoporous carbons as metal-free catalysts for propane dehydrogenation: Effect of the pore structure and surface property*. Chinese Journal of Catalysis 40, 1385-94.

HU Z., ZHENG S., JIA M., DONG X., SUN Z., 2017a. *Preparation and characterization of novel diatomite/ground calcium carbonate composite humidity control material*. Advanced Powder Technology 28, 1372-81.

HU Z., ZHENG S., SUN Z., CHEN Y., YAN Y., 2017b. *Influence of pore structure on humidity control performance of diatomite.* Science and Technology for the Built Environment 23, 1305-13.

HU Z., ZHENG S., TAN Y., JIA M., 2017c. *Preparation and characterization of diatomite/silica composite humidity control material by partial alkali dissolution*. Materials Letters 196, 234-7.

HUO Y., YIN M., RAO Z., 2022. *Heat transfer enhanced by angle-optimized fan-shaped porous medium in phase change thermal energy storage system at pore scale*. International Journal of Thermal Sciences 172, 107363.

IMAMURA H., TABATA S., SHIGETOMI N., TAKESUE Y., SAKATA Y., 2002. *Composites for hydrogen storage by mechanical grinding of graphite carbon and magnesium*. Journal of Alloys, Compounds 330, 579-83.

JIANG D., YUAN Y., WU J., DU Y., WANG J., ZHANG Y., 2019. *Advances in Application of Diatomite-based Composites in the Field of Energy and Environment*. Materials Reports 33(5), 1483-1489.

KHRAISHEH M.A., AL-DEGS Y.S., MCMINN W., 2004. *Remediation of wastewater containing heavy metals using raw and modified diatomite.* Chemical Engineering Journal 99(2),177-184.

KORUNIC Z., 1998. Review *Diatomaceous earths, a group of natural insecticides*. Journal of Stored Products Research 34, 87-97.

LEHMANN A.G., BIONDUCCI M., BUFFA F., 1998. *Effect of mechanical grinding on the hexagonal structure of CdS*e. Physical Review B 58, 5275-81.

LI J., HUANG Q., WANG G., WANG E., 2022. *Influence of active water on gas sorption and pore structure of coal.* Fuel 310, 122400.

LI J., WANG X., WANG J., LI Y., XIA S., ZHAO J., 2019. *Simultaneous recovery of microalgae, ammonium and phosphate from simulated wastewater by MgO modified diatomite*. Chemical Engineering Journal 362, 802-11.

LIU C., ZHANG Y., SUN L., GAO W., JING X., YE W., 2021. *Influence of indoor air temperature and relative humidity on learning performance of undergraduates.* Case Studies in Thermal Engineering 28, 101458.

MANNION A.M., 2012. *The diatoms: applications for the environmental and earth sciences*. Journal of Biological Education 46, 200-1.

MINGMING M.A., ZHANG W., 2017. *Preparation and characterization of diatomite humidity-controlling building material.* New Building Materials.

MU Y., CUI M., ZHANG S., ZHAO J., MENG C., SUN Q., 2018. *Comparison study between a series of new type functional diatomite on methane adsorption performance.* Microporous and Mesoporous Materials 267, 203-11.

OKAMURA C., UEDA T., HASEZAKI K., 2010. *Preparation of Single-Phase ZnSb Thermoelectric Materials Using a Mechanical Grinding Process.* Journal of the Japan Institute of Metals 51, 860-2.

PEDDARASI S., SARKAR D., 2021. *Mechanochemical effect on synthesis and sintering behavior of MgAl2O4 spinel*. Materials Chemistry and Physics 262, 124275.

PYUN S.I., NA K.H., GO J.Y., PARK J.J., 2003. *Characterization of Surface Roughness and Inhomogeneity of Hot-Rolled Carbon Steels by Using Image Analysis Method and Electrochemical Impedance Spectroscopy*. Journal of the Korean Electrochemical Society 6(3), 217-223

QUANG-TUNG, TRAN, TRUNG-DUNG, DANG, ROY, SUDIPTA, BANERJEE, ARGHYA, NARAYAN, 2016. *Fast degradation of dyes in water using manganese-oxide-coated diatomite for environmental remediation*. The journal of physics and chemistry of solids 98, 50-8.

SEOK-HO Y., JONG-BOK N., WON-SEON J., 1989. Effects of Domestic Diatomite Filter Aid on the Characteristics of Cake Filtration. Korean Chemical Engineering Research 27(4), 482.

SERTSUNGNERN P., CHAIWIWATWORAKUL P., 2011. *Development of a Performance Rating Scheme of Air-Conditioning Systems for Buildings: A Case of Thailand*. Energy Procedia 9, 84-94.

SHENG G., WANG S., HU J., YI L., LI J., DONG Y., WANG X., 2009. *Adsorption of Pb(II. on diatomite as affected via aqueous solution chemistry and temperature.* Colloids, Surfaces A Physicochemical, Engineering Aspects 339, 159-66.

SHIH Y.F., WEI C.H., KOTHARANGANNAGARI V.K., 2020. *Study on Reuse of Wasted Diatomite from Brewing Industry for Building Materials*. Key Engineering Materials 845, 73-8.

SONG M.Y., BOBET J.L., DARRIET B., 2002. *Improvement in hydrogen sorption properties of Mg by reactive mechanical grinding with Cr_2O_3, Al_2O_3 and CeO_2*. Journal of Alloys, Compounds 340, 256-62.

SONWANE C.G., BHATIA S.K., CALOS N.J., 1999. Characterization of Surface Roughness of MCM-41 Using Methods of Fractal Analysis. Langmuir 15, 4603-12.

STAMATAKIS M.G., KOUKOUZAS N.K., 2001. The occurrence of phosphate minerals in lacustrine clayey diatomite deposits, Thessaly, Central Greece. Sedimentary Geology 139, 33-47.

THIANGCHANTA S., DO T.A., SUTTAKUL P., MONA Y., 2021. Energy reduction of split-type air conditioners using a pre-cooling system for the condenser. Energy Reports 7, 1-6.

THIANGCHANTA S., DO T.A., TACHAJAPONG W., MONA Y., 2020. *Experimental investigation of the thermoelectric cooling with vacuum wall system.* Energy Reports 6, 1244-8.

VERDUGO R.N., 2008. *Singularities of Geotechnical Properties of Complex Soils in Seismic Regions*. Journal of Geotechnical and Geoenvironmental Engineering 134, 982-91.

VILCHIS-GRANADOS J., GRANADOS-CORREA F., BARRERA-DÍAZ C.E., 2013. *Surface fractal dimensions and textural properties of mesoporous alkaline-earth hydroxyapatites.* Applied Surface Science 279, 97-102.

VU D.H., WANG K.S., BAC B.H., NAM B.X., 2013. *Humidity control materials prepared from diatomite and volcanic ash*. Construction and Building Materials 38, 1066-72.

WANG Y., JIANG Q., JING W., ZHONG Z., XING W., 2022. *Pore structure and surface property design of silicon carbide membrane for water-in-oil emulsification*. Journal of Membrane Science 648, 120347.

WU S., WANG C., JIN Y., ZHOU G., ZHANG L., YU P., SUN L., 2021. *Green synthesis of reusable super-paramagnetic diatomite for aqueous nickel, II. removal*. Journal of Colloid and Interface Science 582, 1179-90.

XIA B.Q., PAN Z.H., YAN J., ZHAO C.Y., 2019. *Mesoscopic exploration on mass transfer in porous thermochemical heat storage materials.* International Journal of Heat and Mass Transfer 135, 52-61.

XIAO Y., LU H.-Q., SHI C.-R., LEI F.-H., RACKEMANN D., LI K., LI W., DOHERTY W.O.S., 2022. *High-performance quaternary ammonium-functionalized chitosan/graphene oxide composite aerogel for remelt syrup decolorization in sugar refining*. Chemical Engineering Journal 428, 132575.

YANG X., LI S., ZHAO J., WANG X., HUANG H., WANG Y., DENG L., 2021. *Development of lithium hydroxide-metal organic framework-derived porous carbon composite materials for efficient low temperature thermal energy storage*. Microporous and Mesoporous Materials 328, 111455.

YUAN P., LIU D., TAN D.-Y., LIU K.-K., YU H.-G., ZHONG Y.-H., YUAN A.-H., YU W.-B., HE H.-P., 2013. *Surface silylation of mesoporous/macroporous diatomite, diatomaceous earth. and its function in Cu(II. adsorption: The effects of heating pretreatment*. Microporous and Mesoporous Materials 170, 9-19.

ZHANG S., ZHAO H., GAO X., ZHAO D., WEI G., LI Z., 2022. *Enhanced surface capacitive sodium storage by pores regulation in carbon/carbon composite nanofibers*. Microporous and Mesoporous Materials 332, 111706.

ZHANG X., LI C., CHEN T., TAN Y., LIU X., YUAN F., ZHENG S., SUN Z., 2021. *Enhanced visible-light-assisted peroxymonosulfate activation over MnFe2O4 modified g-C_3N_4/diatomite composite for bisphenol A degradation.* International Journal of Mining Science and Technology 31(6), 1169-1179.

ZHENG J., SHI J., MA Q., DAI X., CHEN Z., 2017. *Experimental study on humidity control performance of diatomite-based building materials.* Applied Thermal Engineering 114, 450-6.

ZHONG H., WANG J., JIA H., MU Y., LV S., 2019. *Vector field-based support vector regression for building energy consumption prediction*. Applied Energy 242, 403-14.